Driven Hofstadter butterflies and related topological invariants

Martin Wackerl,[*] Paul Wenk,[†] and John Schliemann[‡]
Institute for Theoretical Physics, University of Regensburg, 93040 Regensburg, Germany

(Received 6 February 2018; revised manuscript received 28 August 2019; published 16 October 2019)

The properties of the Hofstadter butterfly, a fractal, self-similar spectrum of a two-dimensional electron gas, are studied in the case where the system is additionally illuminated with monochromatic light. This is accomplished by applying Floquet theory to a tight-binding model on the honeycomb lattice subjected to a perpendicular magnetic field and either linearly or circularly polarized light. It is shown how the deformation of the fractal structure of the spectrum depends on intensity and polarization. Thereby, the topological properties of the Hofstadter butterfly in the presence of the oscillating electric field are investigated. A thorough numerical analysis of not only the Chern numbers but also the W_3 invariants gives the appropriate insight into the topology of this driven system. This includes a comparison of a direct W_3 calculation to the method based on summing up Chern numbers of the truncated Floquet Hamiltonian.

DOI: 10.1103/PhysRevB.100.165411

I. INTRODUCTION

The integer quantum Hall effect [1,2] marks, in hindsight, the inception of the field of topological insulators [3,4]. This discovery was preceded by a few years by Hofstadter's seminal work on hopping models on a two-dimensional square lattice in a perpendicular magnetic field [5]. The celebrated Hofstadter butterfly contains the Landau-level structure underlying the quantum Hall effect in the limit of small fluxes per unit cell. The relation of the band structure to the Hall conductance at general flux was later clarified [6] in terms of Chern numbers [7].

Moreover, an important recent direction of work in the area of topological insulators are systems under external driving, mainly by electromagnetic radiation, and the formation of nontrivial topological phases dubbed Floquet topological insulators [8–16]. In fact, the study of light-matter interaction is one of the fastest growing research areas in physics. Here, two-dimensional systems with underlying honeycomb lattice structure have attracted particular interest including graphene [8,11,17–24], silicene [25,26], germanene [26,27], and transition-metal dichalcogenides [28]. To access, e.g., in graphene the feasibility of AC-driven fields to generate a finite spin polarization of carriers, the effect of periodically driven spin-orbit coupling was studied in Refs. [29,30].

Furthermore, as seen from the quantum Hall effect [2], the topological properties of two-dimensional systems are also drastically altered by applying a perpendicular magnetic field, also leading to fractal structures as the Hofstadter butterfly [5,31–37]. The question arises in which way an external periodic driving can modify or destroy the fractal structure. Moreover, following the seminal paper by Rudner *et al.* [13], it becomes clear that the topology analysis of driven systems needs a different approach compared to the static case which goes beyond the Chern number calculation. We are going to address these problems in the present paper.

Concerning the experimental realizability of the theory developed in this paper, we first emphasize the pioneering work of measuring the Hofstadter butterfly in moiré superlattices [38], showing the possibility of measuring the Hofstadter butterfly on a hexagonal lattice structure as well. Utilizing superlattice structures, the necessary magnetic field can be lowered to easily accessible field strengths of about tens of Tesla. Furthermore, the formation of Floquet bands exists not only on paper. Using angle-resolved photoemission spectroscopy, the periodic band structure was resolved in momentum space and even the gap opening of driven topological insulators was realized and measured [39]. Thus, the path to experimental accessibility is already paved by modern techniques and the study presented in this paper aims at giving a better understanding of the fundamental building blocks by focusing on a single graphene sheet subjected to a strong perpendicular magnetic field and externally driven by polarized light.

This paper is organized as follows. First, we treat in Sec. II the Hofstadter butterfly problem [5] on the honeycomb lattice [31,32,35,40] in a rigorous manner. Then we generalize it in Sec. III to the case with periodic driving, realized by linearly and circularly polarized light. We show some representative numerical results for different frequencies, intensities, and polarizations. Finally, the topological properties of the Floquet-Hofstadter problem are characterized with Chern numbers and W_3 invariants in Sec. IV. Thereby, we compare this invariant with the often-used summation over Chern numbers in the truncated Floquet space for different frequencies and intensities. We combine an analytical as well as a numerical approach to the above quantities, and close with a summary in Sec. V.

[*]martin.wackerl@ur.de
[†]paul.wenk@ur.de
[‡]john.schliemann@ur.de

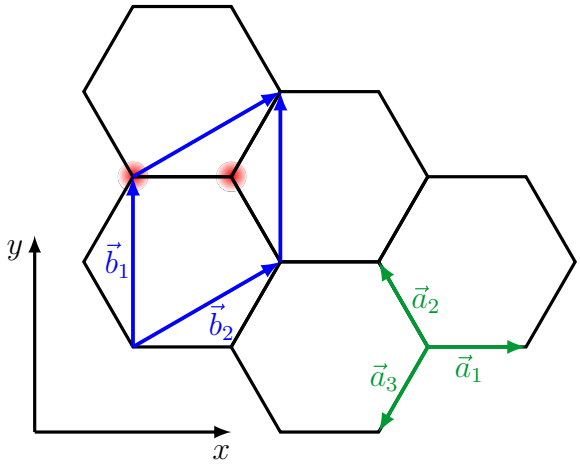

FIG. 1. Coordinate geometry used on the honeycomb lattice: The green arrows represent the different nearest-neighbor vectors $\vec{a}_i$ and the blue ones the lattice vectors $\vec{b}_i$.

II. HOFSTADTER BUTTERFLY FOR THE HONEYCOMB LATTICE

A. Derivation of the Hamiltonian

To model graphene, we use a tight-binding model where only nearest-neighbor hopping can take place. We choose the lattice vectors as

$$\vec{b}_1 = a\begin{pmatrix} 0 \\ \sqrt{3} \end{pmatrix}, \quad \vec{b}_2 = a\begin{pmatrix} \frac{3}{2} \\ \frac{\sqrt{3}}{2} \end{pmatrix}, \tag{1}$$

with a being the distance between the carbon atoms. The nearest-neighbor vectors are

$$\vec{a}_1 = a\begin{pmatrix} 1 \\ 0 \end{pmatrix}, \quad \vec{a}_2 = \frac{a}{2}\begin{pmatrix} -1 \\ \sqrt{3} \end{pmatrix}, \quad \vec{a}_3 = \frac{a}{2}\begin{pmatrix} -1 \\ -\sqrt{3} \end{pmatrix}, \tag{2}$$

as depicted in Fig. 1. The position of an arbitrary unit cell is

$$\vec{R}(m,n) = m\vec{b}_1 + n\vec{b}_2, \quad m,n \in \mathbb{Z}. \tag{3}$$

In the presence of a vector potential, the hopping parameter t gets modified by the Peierls phase,

$$t \mapsto t_{m,n} e^{i\phi^{(j)}_{m,n}}, \tag{4}$$

where the phase is the integral over the vector potential along the hopping path

$$\phi^{(j)}_{m,n} = \frac{e}{\hbar}\int_{\vec{R}(m,n)}^{\vec{R}(m,n)+\vec{a}_j} \vec{A}(\vec{r}\,)\cdot \mathrm{d}\vec{r}, \quad j = 1,2,3\,. \tag{5}$$

The magnetic field is applied in z direction, $\vec{B} = B\vec{e}_z$. For Landau gauge $\vec{A}(\vec{r}\,) = (0, Bx, 0)^T$, the Peierls phase becomes independent of the index m,

$$\int_{\vec{R}(m,n)}^{\vec{R}(m,n)+\vec{a}_{2,3}} \vec{A}(\vec{r}\,)\cdot \mathrm{d}\vec{r} = \pm\frac{3\sqrt{3}}{4}Ba^2\left(n-\frac{1}{6}\right), \tag{6}$$

and zero for the hopping in $\vec{a}_1$ direction. Note that the prefactor in the above expression is related to the area of the elementary unit cell A_{cell} by $3\sqrt{3}a^2/4 = A_{\mathrm{cell}}/2$. As usual, we restrict the flux per unit cell in units of the elementary charge over Planck's constant to a rational value:

$$\phi \equiv \frac{e}{h}BA_{\mathrm{cell}} = \frac{p}{q}. \tag{7}$$

Thus, the Peierls phase can be written as

$$\frac{e}{\hbar}\frac{3\sqrt{3}}{4}Ba^2\left(n-\frac{1}{6}\right) = \pi\phi\left(n-\frac{1}{6}\right), \tag{8}$$

which leads then to the explicit form of of the Hamiltonian

$$H = -t\sum_{mn}\big[a^\dagger_{m,n}\big(b_{m,n} + e^{i\pi\phi(n-\frac{1}{6})}b_{m+1,n-1} + e^{-i\pi\phi(n-\frac{1}{6})}b_{m,n-1}\big) + \mathrm{H.c.}\big], \tag{9}$$

where the sum is over all unit cell positions. The solutions of the stationary Schrödinger equation are plane-wave type states of the general form

$$|\vec{k}\rangle = \sum_{mn} e^{i\vec{k}\cdot\vec{R}(m,n)}(\alpha_n a^\dagger_{m,n} + \beta_n b^\dagger_{m,n})|0\rangle, \tag{10}$$

where the creation operators $a^\dagger_{m,n}, b^\dagger_{m,n}$ for the different sublattice sites are acting on the fermionic vacuum $|0\rangle$. α_n, β_n are complex amplitudes depending only on n since the Peierls phase does so, see Eq. (8). Making a projection on a state $\langle 0|a_{m',n'}$ or $\langle 0|b_{m',n'}$ leads to a system of coupled equations for the amplitudes,

$$-\frac{\varepsilon}{t}\alpha_n = \beta_n + z_n(\vec{k})\beta_{n-1}, \tag{11}$$

$$-\frac{\varepsilon}{t}\beta_n = \alpha_n + z^*_{n+1}(\vec{k})\alpha_{n+1}, \tag{12}$$

with

$$z_n(\vec{k}) = e^{-i\pi\phi(n-\frac{1}{6})-i\vec{k}\cdot\vec{b}_2} + e^{i\pi\phi(n-\frac{1}{6})}e^{i\vec{k}\cdot(\vec{b}_1-\vec{b}_2)}. \tag{13}$$

B. Periodicity of the Hofstadter Problem

Equations (11) and (12) define a prima vista infinite system of linear equation, which, however, closes to a finite one due to periodicity properties of the amplitudes involved. First, we define the operators

$$T_r\begin{pmatrix} a_{m,n} \\ b_{m,n} \end{pmatrix}T_r^\dagger = \begin{pmatrix} a_{m,n+r} \\ b_{m,n+r} \end{pmatrix}, \tag{14}$$

$$u\begin{pmatrix} a_{m,n} \\ b_{m,n} \end{pmatrix}u^\dagger = (-1)^n\begin{pmatrix} a_{m,n} \\ b_{m,n} \end{pmatrix}, \tag{15}$$

such that for

$$p \text{ even:} \quad T_q H T_q^\dagger = H, \tag{16}$$

$$p \text{ odd:} \quad uT_q H T_q^\dagger u^\dagger = H. \tag{17}$$

For even p, the translation operator T_q acts on the state ansatz as

$$|\vec{k}\rangle = e^{i\vec{k}\cdot\vec{b}_2 q}\,T_q\,|\vec{k}\rangle\,, \tag{18}$$

and consequently the amplitudes have the periodicity

$$\alpha_{n+q} = \alpha_n, \quad \beta_{n+q} = \beta_n\,. \tag{19}$$

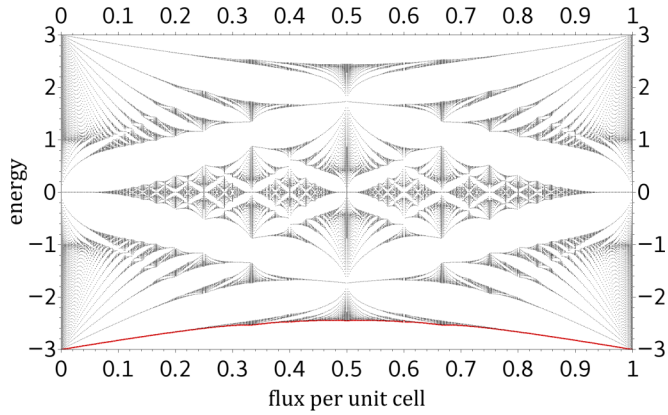

FIG. 2. Hofstadter butterfly for the honeycomb lattice. The energy is given in units of the hopping parameter t.The ground state of the Hofstadter spectrum is defined as the state with lowest energy, represented by the red line.

In the other case where p is odd,

$$|\vec{k}\rangle = e^{i\vec{k}\cdot\vec{b}_2 q}\, uT_q\, |\vec{k}\rangle\,, \tag{20}$$

and the amplitudes have to fulfill

$$\alpha_{n+q} = (-1)^{n+q}\alpha_n, \quad \beta_{n+q} = (-1)^{n+q}\beta_n. \tag{21}$$

The relations given in Eqs. (19) and (21) can be summarized as

$$\alpha_q = (-1)^{pq}\alpha_0, \quad \beta_q = (-1)^{pq}\beta_0. \tag{22}$$

Thus, Eqs. (11) and (12) define a finite linear system of equation for, say, $\alpha_0 \ldots \alpha_{q-1}$ and $\beta_0 \ldots \beta_{q-1}$, and if both p and q are odd the relation between the missing amplitudes α_q, β_q and α_0, β_0, respectively, contains an additional minus sign. This sign can be compensated by shifting the wave vectors by half of a reciprocal lattice vector as $k_x \to k_x + \frac{2\pi}{3q}$, leading to

$$\alpha_{n+q} = (-1)^{n+1+q}\alpha_n\,, \tag{23}$$

$$\beta_{n+q} = (-1)^{n+1+q}\beta_n\,. \tag{24}$$

This allows us to use Eqs. (19) for all flux values in the calculation of the Hofstadter spectrum and Chern numbers but one should keep in mind that one gets a shifted band structure for odd flux values according to Eqs. (20)–(24). As a result, to calculate the Hofstadter butterfly, a $2q \times 2q$ matrix is sufficient to obtain the full Hofstadter spectrum. The numerical result for various fluxes is depicted in Fig. 2.

III. FLOQUET-HOFSTADTER SPECTRUM

In this section, we generalize the Hofstadter butterfly to the case of an additional oscillating electric field. We will focus on linear and circular polarization and show how the two polarization states affect the Hofstadter spectrum.

A. Circularly polarized light

The following vector potential $\vec{A}$ is representing circularly polarized light of frequency ω in the xy-plane and amplitude A, and the perpendicular magnetic field B:

$$\vec{A}(\vec{r},t) = \begin{pmatrix} A\sin(\omega t) \\ A\cos(\omega t) + Bx \end{pmatrix}. \tag{25}$$

The vector potential is included in the Hamiltonian via Peierls substitution. In what follows, the hopping parameter is renamed g, and $\vec{A}(t)$ is representing only the time-dependent part of Eq. (25). The resulting Hamiltonian reads

$$H = -g\sum_{mn}\Big[a^\dagger_{m,n}\Big(\, e^{i\frac{e}{\hbar}\vec{A}(t)\cdot\vec{a}_1} b_{m,n} + e^{i\pi\phi(n-\frac{1}{6})+i\frac{e}{\hbar}\vec{A}(t)\cdot\vec{a}_2} b_{m+1,n-1} + e^{-i\pi\phi(n-\frac{1}{6})+i\frac{e}{\hbar}\vec{A}(t)\cdot\vec{a}_3} b_{m,n-1}\Big) + \text{H.c.}\Big]. \tag{26}$$

The time-dependent Schrödinger equation can be expressed in the Floquet form,

$$H_F\,|\vec{k},t\rangle := (H - i\hbar\partial_t)\,|\vec{k},t\rangle = \varepsilon\,|\vec{k},t\rangle\,, \tag{27}$$

where ε is the quasienergy which is only defined modulo integer multiples of $\hbar\omega$. The state $|\vec{k},t\rangle$ is periodic in time with a period $T = 2\pi/\omega$ which allows for a discrete Fourier transformation. According to Eq. (10), the general solution of H_F can be written in the form

$$|\vec{k},t\rangle = \sum_{mn} e^{i\vec{k}\cdot\vec{R}(m,n)}(\alpha_n(t)a^\dagger_{m,n} + \beta_n(t)b^\dagger_{m,n})|0\rangle. \tag{28}$$

Due to the periodicity of $|\vec{k},t\rangle$, one can expand the terms $\alpha_n(t)$, $\beta_n(t)$ using the Fourier series

$$\alpha_n(t) = \sum_l \alpha_{n,l} e^{il\omega t}, \tag{29}$$

where the index l is the quantum number of the Floquet mode (also called Floquet replica). The equivalent to Brillouin zones (BZs) for the real space are the Floquet modes for the time space. Additionally, we use the Jacobi-Anger expansion [24],

$$e^{iz\cos(\omega t)} = \sum_{n=-\infty}^{\infty} J_n(z) e^{in(\omega t+\frac{\pi}{2})}, \tag{30}$$

where J_n denotes the nth order Bessel function of the first kind. The Floquet Eq. (27) leads to the following coupled expressions for the amplitudes:

$$l\hbar\omega\alpha_{n,l} - g\sum_{l'} J_{l'}(\gamma)[\beta_{n,l-l'} + f_{n,l'}(\vec{k})\beta_{n-1,l-l'}] = \varepsilon\alpha_{n,l}, \tag{31}$$

$$l\hbar\omega\beta_{n,l} - g\sum_{l'} J_{l'}(\gamma)[\alpha_{n,l+l'} + f^*_{n+1,l'}(\vec{k})\alpha_{n+1,l+l'}] = \varepsilon\beta_{n,l}, \tag{32}$$

with

$$f_{n,l'}(\vec{k}) = e^{i\pi\phi(n-\frac{1}{6})-il'\frac{4\pi}{3}} e^{i\vec{k}\cdot(\vec{b}_1-\vec{b}_2)} + e^{-i\pi\phi(n-\frac{1}{6})-il'\frac{2\pi}{3}} e^{-i\vec{k}\cdot\vec{b}_2}, \tag{33}$$

where $\gamma \equiv eAa/\hbar$, termed light parameter. Exemplary numerical results for different driving frequencies can be seen in Figs. 3 and 4. The bending direction represented by the green dashed line depends on the sign of the driving frequency ω.

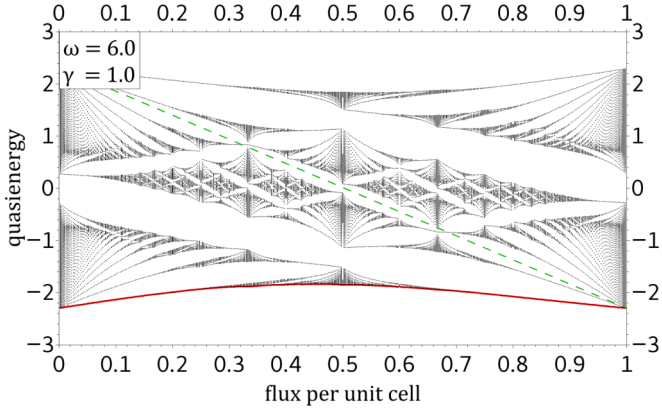

FIG. 3. The Hofstadter butterfly gets deformed in the presence of circularly polarized light. The frequency ω of the periodic driving was set to $6.0\,g/\hbar$ and the intensity γ to $1.0\,eAa/\hbar$. With the present choice of frequency, the different butterflies of the different Floquet modes do not overlap. The red line shows the state with lowest quasienergy of the central Floquet mode.

B. Linearly polarized light

We now investigate the case of linear polarization of the light represented by

$$\vec{A}(\vec{r},t) = \begin{pmatrix} A_x \cos(\omega t) \\ A_y \cos(\omega t) + Bx \end{pmatrix}. \tag{34}$$

The orientation of the linear polarization can be tuned by varying A_x and A_y. The effective amplitude for the three different hopping paths is then governed by

$$\vec{A}(t)\cdot\vec{a}_i = A_i \cos(\omega t) \quad \text{with} \quad i = 1,2,3\,. \tag{35}$$

In contrast to the case of circularly polarized light, where the transitions between the different Floquet modes are for all hopping directions equally suppressed, they are for linear polarization not. This can be seen from the fact that the argument of the Bessel function is different for each hopping

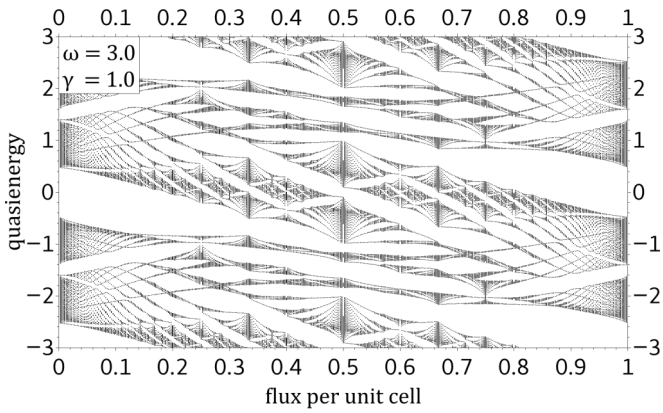

FIG. 4. The frequency ω of the circularly polarized radiation was set to $3.0\,g/\hbar$ and the intensity γ to $1.0\,eAa/\hbar$. The spectra of the different Floquet modes overlap.

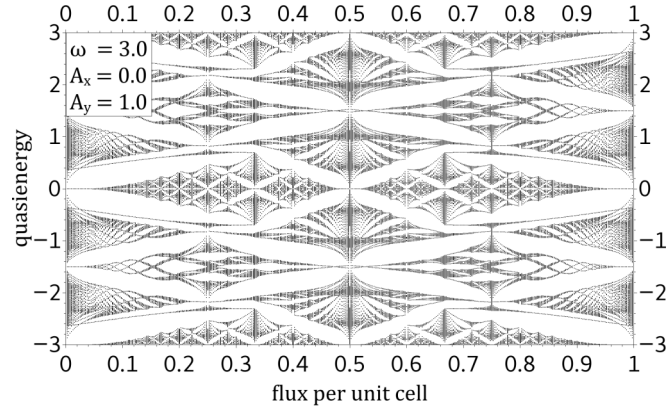

FIG. 5. Hofstadter butterfly in the presence of linearly polarized light where $A_x = 0.0$, $A_y = 1.0$ at a frequency ω of $3.0\,g/\hbar$. The effective amplitude for each hopping direction is governed by Eq. (35).

direction. The equivalent equations to Eqs. (31) and (32) for linearly polarized light read

$$l\hbar\omega\alpha_{n,l} - g\sum_{l'}\Big[\big(J_{l'}(\gamma_1)\beta_{n,l-l'} + J_{l'}(\gamma_2)e^{i\pi\phi(n-\frac{1}{6})+i\vec{k}\cdot(\vec{b}_1-\vec{b}_2)} + J_{l'}(\gamma_3)e^{-i\pi\phi(n-\frac{1}{6})-i\vec{k}\cdot\vec{b}_2}\big)\beta_{n-1,l-l'}\Big] = \varepsilon\alpha_{n,l}, \tag{36}$$

$$l\hbar\omega\beta_{n,l} - g\sum_{l'}\Big[\big(J_{l'}(\gamma_1)\alpha_{n,l+l'} + J_{l'}(\gamma_2)e^{-i\pi\phi(n+\frac{5}{6})-i\vec{k}\cdot(\vec{b}_1-\vec{b}_2)} + J_{l'}(\gamma_3)e^{i\pi\phi(n+\frac{5}{6})+i\vec{k}\cdot\vec{b}_2}\big)\alpha_{n+1,l+l'}\Big] = \varepsilon\beta_{n,l}. \tag{37}$$

Here, we have introduced three different light parameters:

$$\gamma_i = \frac{eA_i a}{\hbar}\,.$$

One should note that particle-hole symmetry is conserved for linear light polarization, see Fig. 5, whereas it is not for circular polarization.

C. Gap size

To prepare for the following section, where we analyze the Chern numbers of the static Hofstadter and the Floquet-Hofstadter problem, we investigate the gap size occurring between the different Floquet-Butterfly modes. To do so, we first clarify what is meant by the gap between the different butterflies. We always calculate the gap size numerically between the lowest band of the central Floquet mode, being in the interval $[-\hbar\omega/2, \hbar\omega/2)$, and the highest band of the minus one Floquet mode, lying in $[-3\hbar\omega/2, -\hbar\omega/2)$. Due to the periodicity of the Floquet-Hofstadter spectrum on the quasienergy axis, the gap between neighboring modes is always the same. It is obvious that the quasienergetic gap is not equal for all flux values, e.g., in Fig. 3 the lowest band of the central Floquet mode is not constant as a function of the flux per unit cell.

As already mentioned, we focus on Chern numbers in the following section. A change of the Chern number is always related to a band touching. Hence, we are interested in the minimal gap as a function of flux, denoted as $\Delta\varepsilon$ in Figs. 6, 7, and 8. We refer to a gap between the butterflies if there is no flux value where the lowest band of the central Floquet

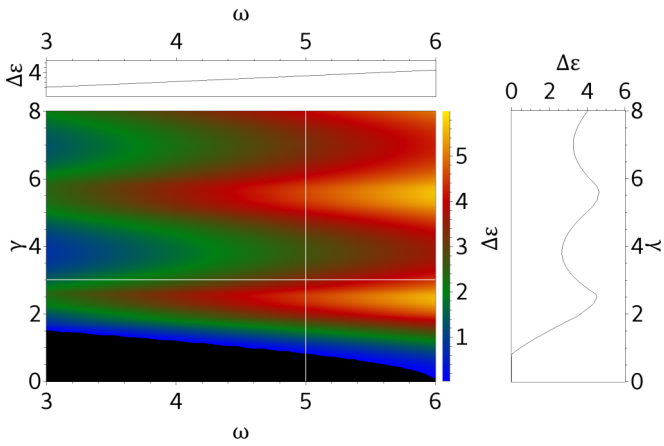

FIG. 6. The gap $\Delta\epsilon$ of the Floquet-Hofstadter spectrum as a function of frequency ω and intensity γ for circularly polarized light. In the investigated intensity range, two maxima occur rising linearly with the driving frequency.

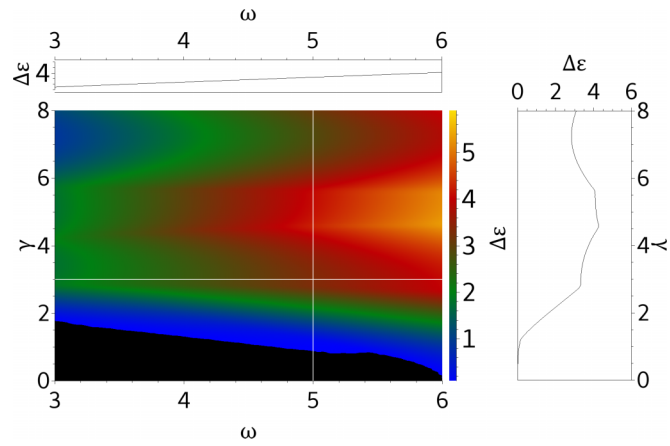

FIG. 8. The polarization was set in x direction, parallel to the $\vec{a}_1$ bonding. The two gap maxima at $\gamma = 2.75\,eAa/\hbar$ and $\gamma = 6.4\,eAa/\hbar$ at $\omega = 5.0\,g/\hbar$ for y polarization move together when changing the polarization into the x direction.

mode and the highest band of the $n = -1$ mode touch. The right plots of Figs. 6, 7, and 8 show cuts through the contour plot at a frequency of $5.0\,g/\hbar$. The upper plots show cuts at an intensity of $3.0\,eAa/\hbar$. We can see that the gap size rises linearly with the frequency. In anticipation of the following section, we can state that the change of Chern numbers for $\omega = 6.0\,g/\hbar$ is for all polarizations only induced by band touchings of butterfly bands lying in the same Floquet zone and not by touching of bands from different Floquet modes.

IV. TOPOLOGICAL CHARACTERIZATION

A. Chern numbers

Now we turn to the topological characterization of the Hofstadter bands [6,24,41–43], focusing first on Chern numbers. The topological invariants can be defined for quantum states with two periodic parameters. They are calculated by an integral of the Berry curvature $\vec{F}$ over a two-dimensional compact surface $\mathcal{T}^2$, in this case the BZ in the quasienergy space of H_F: Since the eigenstate $|\alpha, \vec{k}, t\rangle$ with $H_F\,|\alpha, \vec{k}, t\rangle = \varepsilon_\alpha\,|\alpha, \vec{k}, t\rangle$ is periodic in time we can, according to Eq. (29), also formally write

$$|\alpha, \vec{k}, t\rangle = \sum_n e^{in\omega t}\,\left|u^n_{\vec{k}\alpha}\right\rangle, \tag{38}$$

where α refers to a band index within one Floquet replica n. The Chern number associated to a Floquet band α with a Floquet state $|u^n_{\vec{k}\alpha}\rangle$ and quasienergy $\varepsilon_{\vec{k}\alpha}$ is given by

$$C_\alpha = \frac{1}{2\pi}\int_{\mathrm{BZ}} d^2k\,\vec{F}_\alpha(\vec{k})\cdot\hat{z}, \tag{39}$$

with the Berry curvature [6,44,45] given by

$$\vec{F}_\alpha(\vec{k}) = \sum_{\beta\neq\alpha}\mathrm{Im}\frac{\left\langle u^n_{\vec{k}\alpha}\right|\vec{\nabla}_{\vec{k}}H_F\left|u^n_{\vec{k}\beta}\right\rangle \times \left\langle u^n_{\vec{k}\beta}\right|\vec{\nabla}_{\vec{k}}H_F\left|u^n_{\vec{k}\alpha}\right\rangle}{(\varepsilon_{\vec{k}\alpha}-\varepsilon_{\vec{k}\beta})^2}. \tag{40}$$

As long as the Floquet space is not truncated, $\vec{F}_\alpha(\vec{k})$ does not depend on the Floquet mode n. The effect of a truncation of the Floquet space will be discussed in Sec. IV B.

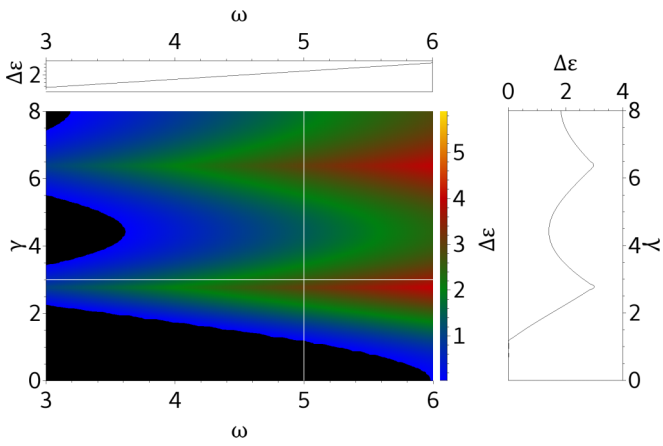

FIG. 7. The polarization shows in y direction. The gap shows qualitatively a similar behavior as for circularly polarized light but the gap is overall smaller.

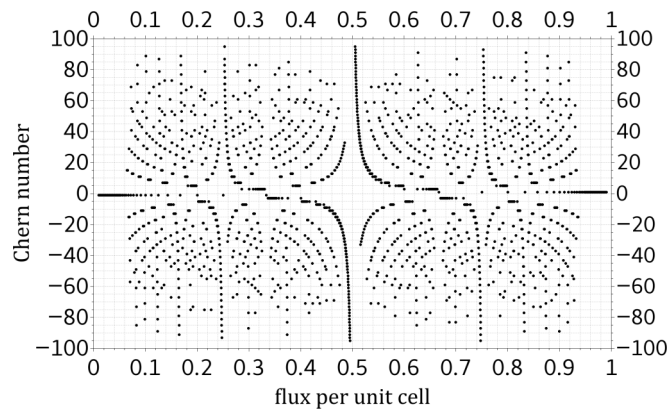

FIG. 9. The Chern number of the state of lowest energy of the Hofstadter butterfly in dependence of the magnetic flux per unit cell. The flux values are all p/q with p coprime to $q < 101$.

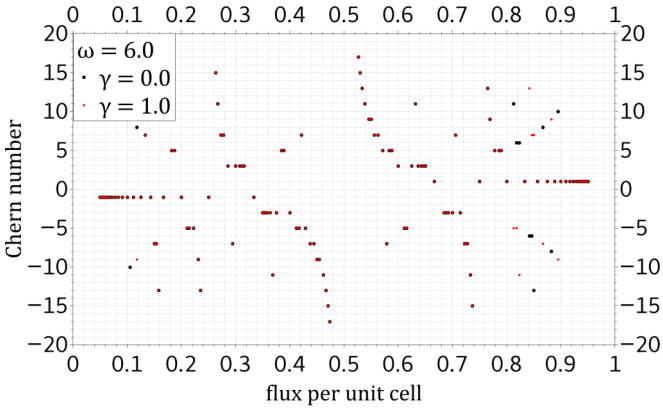

FIG. 10. The ground-state Chern number of the Floquet-Hofstadter spectrum: The frequency ω of the circularly polarized light was set to 6.0 $g/\hbar$. The black values show the case of vanishing light intensity γ and the red values are calculated for an intensity of 1.0 $eAa/\hbar$.

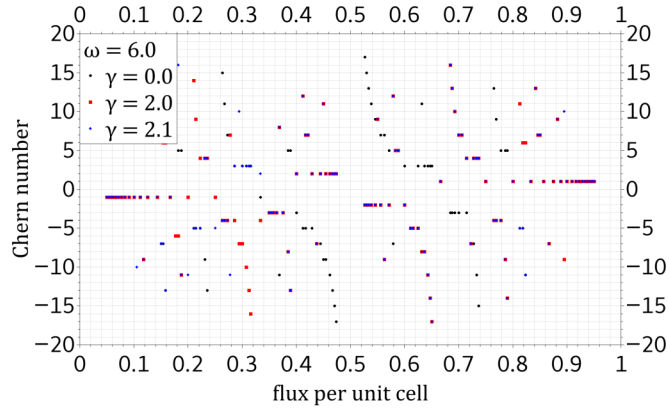

FIG. 11. The distribution of the ground state Chern number in the presence of circularly polarized light exhibits, for intensities γ of 2.0 $eAa/\hbar$ and 2.1 $eAa/\hbar$, a rather different behavior as for vanishing intensity. The plot shows flux values for $q < 21$.

Following Goldman [46], we concentrate on the state of lowest energy in one Floquet mode at given flux per unit cell as indicated in Fig. 2. The Chern number is calculated numerically by the method proposed by Fukui *et al.* [7]. Figure 9 reproduces the data of Ref. [46] and extends it to a larger number of different flux values $\phi = p/q$. The computation is effectively limited by the fact that with growing q (being coprime to p), energy bands move closer to each other and are increasingly difficult to resolve, an effect which is most pronounced at fluxes near zero and unity. From a numerical perspective, the bands are degenerate, impeding the use of the computation scheme by Fukui *et al.* constructed for nondegenerate band structures.

Next, we analyze how polarized light affects the Chern numbers of the Hofstadter butterfly. First, let us consider the case of circularly polarized light. The basis for this analysis is Eqs. (31) and (32). At high frequencies the Hofstadter butterflies of the different Floquet modes are quasienergetically separated since the distance of the Floquet modes is governed by the photon energy. Hence, the change of Chern numbers is induced by band touchings within the Floquet zone, as can be seen in Figs. 6, 7, and 8. At frequencies large compared to the hopping energy, the butterfly spectrum has an overall gap in a broad intensity range. For intensities considered in this section, the topological phase transitions are all due to band touchings within the same Floquet mode. Again, we concentrate on the state of lowest quasienergy in the central Floquet mode, see Fig. 3. With Eqs. (31) and (32), we were able to reproduce several results of Mikami *et al.* [14] in the limit of vanishing magnetic field strength.

As already stressed in several works [14,47,48], the distribution function in a driven system is in general not an equilibrium distribution function. Despite that, the Chern number maintains its significance [14], keeping in mind that one needs another topological invariant to fully characterize a driven system [13]. We use the term *ground state* as the state with lowest quasienergy of the central Floquet mode, emphasizing that we do not touch the question of the occupation of the Floquet modes in general. However, we assume that the ground state depends adiabatically on the intensity at least in the high frequency regime. As long as the driving is far from resonances the driving does not significantly change the ground state and with that the distribution function. This also requires that the driving must not induce a heating of the system. Hence, if we only occupy the ground state of the static system, we also assume that in the off-resonantly driven system only the ground state is occupied.

Our Chern number computations are done in the off-resonant frequency regime. Hence, the ground state of the driven system undergoes the topological phase transitions presented in Figs. 10, 11, and 12. For a vanishing light parameter γ and high frequencies, the ground-state Chern numbers are the same as in the undriven case, see Fig. 9. In Fig. 10, most Chern numbers coincide with the case of a vanishing intensity. When the intensity is further increased, the ground-state Chern number exhibits a rather different behavior. Even small intensity changes can have a vast influence on the Chern number [14], see Fig. 11. Since the Floquet-Hofstadter spectrum gets twisted in the presence of circularly polarized light and keeps particle-hole symmetry for linearly polarized light,

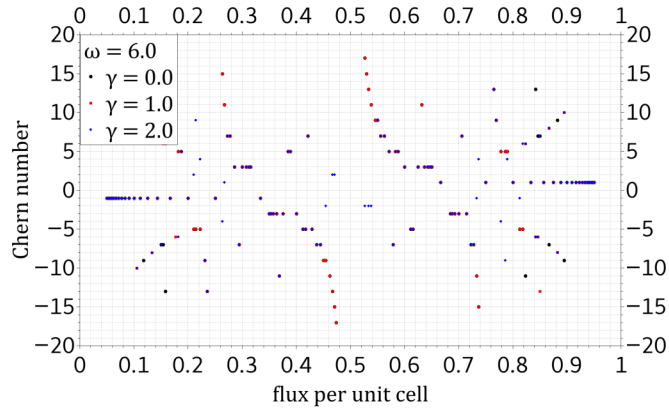

FIG. 12. In the case of linear polarization with $A_x = 0.0, A_y = \gamma$, the distribution of the Chern number is for linearly polarized light similarly affected as for circularly polarized light. The frequency ω was again fixed at 6.0 $g/\hbar$ and the intensity is governed by Eq. (35).

it is obvious that the band structure of graphene is affected differently for the two polarization states. The deformation of the band structure and the associated gap closing and opening is related to the change of Chern numbers. Hence, we also investigate the influence of linearly polarized light on the distribution of Chern numbers. Similar to the case of circularly polarized light, for rather small intensities only few Chern numbers deviate from the static Chern number distribution. An increase of the intensity leads to a significantly different behavior, as shown in Fig. 12. For circularly polarized light, the ground state is uniquely defined. Whereas, for linearly polarized light this is not the case for all flux values. At flux values of, e.g., 6/11, 6/13, or 3/17, a band crossing of the ground state occurs. This effect can be seen at eight different flux values for $q < 21$. The occurrence of the band crossing of the ground state seems not to follow a simple rule.

B. W_3 invariants

The topological invariant ν_3 associated with the third homotopy group of the periodic unitary maps $\{U_{\vec{k}}(T)\}$ is given in $\mathbb{R}^3$ by

$$\nu_3[U_{\vec{k}}] = \frac{1}{24\pi^2}\int_{\mathrm{BZ}} d^3k\,\varepsilon_{\alpha\beta\gamma}\,\mathrm{tr}\big[\big(U_{\vec{k}}^{-1}(T)\partial^\alpha U_{\vec{k}}(T)\big)\cdot\big(U_{\vec{k}}^{-1}(T)\partial^\beta U_{\vec{k}}(T)\big)\big(U_{\vec{k}}^{-1}(T)\partial^\gamma U_{\vec{k}}(T)\big)\big]. \tag{41}$$

Rudner *et al.* [13] have devised an invariant specifically designed for the characterization of periodically driven systems. The idea is to replace in Eq. (41) one k-dimension with the time and choose a unitary matrix $\tilde{U}_{\vec{\mu}}$ which is periodic in time and topologically equivalent to a time evolution operator $U_{\vec{\mu}}$[49],

$$W_3[\tilde{U}_{\vec{\mu}}] = \frac{1}{24\pi^2}\int_{[0,1)^3} d^3\mu\,\varepsilon_{\alpha\beta\gamma}\,\mathrm{tr}\big[\big(\tilde{U}_{\vec{\mu}}^{-1}\partial^\alpha\tilde{U}_{\vec{\mu}}\big)\cdot\big(\tilde{U}_{\vec{\mu}}^{-1}\partial^\beta\tilde{U}_{\vec{\mu}}\big)\big(\tilde{U}_{\vec{\mu}}^{-1}\partial^\gamma\tilde{U}_{\vec{\mu}}\big)\big], \tag{42}$$

where the cube $[0,1)^3$ is spanned by two normalized in-plane wave vectors and the time t/T with $\vec{\mu}\in[0,1)^3$. The indices α,β,γ are given modulo 3 and $\partial^\alpha \equiv \partial^{\mu_\alpha}$. This new invariant is related to the lowest quasienergy gap in the central Floquet mode. The relation between the W_3 invariants of different gaps ξ_n with $\exp(i\xi_n)\in\mathbb{S}^1$ around quasienergies ε_ν is closely related to Chern numbers C^ν of appropriate bands ν. It is given by [42]

$$W_3[\tilde{U},\xi_b] = W_3[\tilde{U},\xi_a] - \sum_{\nu=\nu_1,\ldots,\nu_k} C_\nu^{(3)}\Big|_{\mu_3\equiv\frac{t}{T}=1}, \tag{43}$$

where the bands $\nu_1,\ldots,\nu_k$ are the bands one passes through when the value ξ changes from the gap at $\xi=\xi_a$ to the gap at $\xi=\xi_b$. The Chern number is calculated by [42]

$$C_\nu^{(\alpha)} = \frac{1}{2\pi i}\int_0^1\int_0^1 d\mu_{\alpha-1}d\mu_{\alpha+1}\,[\varepsilon_{\alpha\beta\gamma}(\partial^\beta(S^\dagger\partial^\gamma S))]_{\nu\nu}, \tag{44}$$

where $C_\nu^{(3)}|_{\mu_3=1}$ is equivalent to Eq. (39). The columns of the matrix S contain the eigenvectors of $U_{\vec{\mu}}$. Clearly, the full computation of the invariant constructed in Ref. [13] is more complicated [42] than for Chern numbers [7].

The calculation scheme suggested by Rudner *et al.* [13] in frequency space is described in the following. To calculate the generalized topological invariant for driven systems, one first computes the Chern number of all bands below the investigated gap of a truncated Floquet matrix. The generalized invariant is then given by the sum off all Chern numbers below this gap. In Fig. 5 in Ref. [13], the lowest band of the truncated Floquet matrix has a Chern number C_0 different from C_F. The reason why that Chern number is not C_F is due to the truncation. As already shown by Shirley [50,51] from the Fourier expansion in Eq. (38), it follows that the corresponding eigenvector to a quasienergy ε_λ differs from the eigenvector of the quasienergy $\varepsilon_\lambda+\hbar\omega$ only by an index shift of the entries and a phase ϕ, which one is free to choose [50],

$$\varepsilon_\lambda \leftrightarrow \begin{pmatrix}\vdots\\ u_\lambda^{-2}\\ u_\lambda^{-1}\\ u_\lambda^{0}\\ u_\lambda^{1}\\ u_\lambda^{2}\\ \vdots\end{pmatrix} \Longleftrightarrow \varepsilon_\lambda+\hbar\omega \leftrightarrow e^{i\phi}\begin{pmatrix}\vdots\\ u_\lambda^{-3}\\ u_\lambda^{-2}\\ u_\lambda^{-1}\\ u_\lambda^{0}\\ u_\lambda^{1}\\ \vdots\end{pmatrix}, \tag{45}$$

where λ labels a discrete set of quantum numbers, e.g., spin or sublattice degrees. This holds equivalently for arbitrary shifts $n\hbar\omega$, with $n\in\mathbb{Z}$, of the quasienergy. It shows that the Chern number C_{ε_λ} of a band described by ε_λ has to be equal to the Chern number of the shifted band:

$$C_{\varepsilon_\lambda} = C_{\varepsilon_\lambda+n\hbar\omega}\,. \tag{46}$$

This means for the numerics that if we assume that only a finite number of eigenvector entries are different from zero, we have to choose the truncation of the Floquet modes large enough to achieve convergence of these. Let us assume that we have to limit the number of Floquet modes to m to achieve convergence of the central quasienergy ε_λ up to a needed precision. If the eigenvector corresponding to $\varepsilon_\lambda\pm m\hbar\omega$ is computed, the eigenvalues and eigenvectors are in general not converged, leading to different results in the quasienergy spectrum as well as Chern numbers. To sum up, these nonconverged Chern numbers might lead to an incorrect topological characterization. Indeed, Höckendorf *et al.* give a counterexample in Ref. [42] where the summation over Chern numbers suggested by Rudner *et al.* [13] fails to give the correct W_3 invariant. The authors consider a spin-1/2 rotation described by the Hamiltonian

$$H_w = 2\pi w\,\vec{f}(\mu_1,\mu_2)\cdot\vec{\sigma}, \tag{47}$$

together with the corresponding time-evolution operator

$$U(\vec{\mu}) = e^{-iH\mu_3}, \tag{48}$$

where the μ_i are chosen as in Eq. (42), $w\in\mathbb{Z}$ and the function $\vec{f}$ is a map from the square to the unit sphere $\vec{f}:[0,1]^2\to\mathbb{S}^2$. For further details, we refer to Ref. [42]. The corresponding two bands have Chern number ±1, whereas

$W_3 = 2w$. Despite the fact that the Hamiltonian H is time independent, the system exhibits a nontrivial topology when investigating its time evolution. We are now in the position to clarify why the summation over Chern numbers proposed by Rudner *et al.* fails for this example. If we apply Floquet theory to the Hamiltonian Eq. (47) with vanishing driving amplitude and frequency $\omega = 2\pi/T$, we create Floquet copies identical to the undriven system. This implies that the Chern numbers of the two bands in each Floquet zone are equal to the Chern numbers of the undriven system, i.e., they are ± 1. Therefore, summing over all Floquet copies yields a topological invariant of zero in contrast to the correct W_3 invariant of $2w$. The above mapping $\vec{f}(\mu_1, \mu_2)$ can be easily constructed by concatenating three different mappings. The first one is shifting and stretching the square:

$$\vec{s}(\vec{\mu}) : [0, 1]^2 \to [-1, 1]^2, \tag{49}$$

$$\vec{s}(\vec{\mu}) : \begin{pmatrix} \mu_1 \\ \mu_2 \end{pmatrix} \mapsto \begin{pmatrix} 2\mu_1 - 1 \\ 2\mu_2 - 1 \end{pmatrix}. \tag{50}$$

The second one is a map from a square to a circle,

$$\vec{c}(\vec{\mu}) : [-1, 1]^2 \to \{|\vec{\mu}| \leqslant 1 : \vec{\mu} \in \mathbb{R}^2\}, \tag{51}$$

$$\vec{c}(\vec{\mu}) : \begin{pmatrix} \mu_1 \\ \mu_2 \end{pmatrix} \mapsto \begin{pmatrix} \mu_1 \sqrt{1 - \frac{\mu_2^2}{2}} \\ \mu_2 \sqrt{1 - \frac{\mu_1^2}{2}} \end{pmatrix}, \tag{52}$$

and the third one maps a circle to a sphere,

$$\vec{b}(\vec{\mu}) : \{|\vec{\mu}| \leqslant 1 : \vec{\mu} \in \mathbb{R}^2\} \to \{|\vec{\mu}| = 1 : \vec{\mu} \in \mathbb{R}^3\}, \tag{53}$$

$$\vec{b}(\vec{\mu}) : \begin{pmatrix} \mu_1 \\ \mu_2 \end{pmatrix} \mapsto \begin{pmatrix} \frac{\mu_1}{n} \sin(\pi n) \\ \frac{\mu_2}{n} \sin(\pi n) \\ \cos(\pi n) \end{pmatrix}, \tag{54}$$

with $n = \sqrt{\mu_1^2 + \mu_2^2}$. This finally yields the sought mapping f:

$$\vec{f}(\mu_1, \mu_2) = \vec{b}(\vec{c}(\vec{s}(\vec{\mu}))) . \tag{55}$$

Let us now consider the case $w = 1$. The operator in Eq. (48) can be interpreted as a time-evolution operator of a time-independent Hamiltonian,

$$H_{w=1} = \frac{2\pi}{T} \vec{f}(\mu_1, \mu_2) \cdot \vec{\sigma}, \tag{56}$$

which has, however, a trivial but periodic time evolution with a period $T = 1$. Note that the eigenvector matrix Λ of $H_{w=1}$ allows for the transformation:

$$\Lambda \vec{f}(\mu_1, \mu_2) \cdot \vec{\sigma} \Lambda^\dagger = \sigma^z. \tag{57}$$

Rudner *et al.*, Appendix C in Ref. [13], made the attempt to map all time-independent flat-band Hamiltonians onto

$$H_P(\vec{\mu}) = \frac{2\pi}{T} P(\vec{\mu}), \tag{58}$$

with $P(\vec{\mu})$ being a projection operator. The authors were able to show that for these class of Hamiltonians the W_3-invariant $W_3[U]$ is equal to the Chern number of the bands with quasienergy $\varepsilon = -2\pi/T$. One should stress that the quasienergies of a Hamiltonian of the form Eq. (58) are degenerate everywhere whereas the Chern numbers are still defined. But there is a class of flat-band Hamiltonians which cannot be mapped onto H_P. One example is $H_{w=1}$ since the spectra differ. Here, the mentioned relation between the W_3 invariant and the Chern number fails. Furthermore, very much as in Appendix C, one can show that the quasienergies of the Floquet Hamiltonian corresponding to Eq. (56) are both zero and thus degenerate everywhere. Nevertheless, the Chern numbers are ± 1 and summation over these will never lead to the same number of edge modes as predicted by $W_3 = 2$. This shows that the summation over Chern numbers of the truncated Floquet Hamiltonian is not justified for every system. Another example is discussed in Appendix C. Despite these counterexamples, the summation over Chern numbers over the truncated Floquet matrix and the calculation of the W_3 invariant for graphene without magnetic field show a striking accordance, see Appendix B.

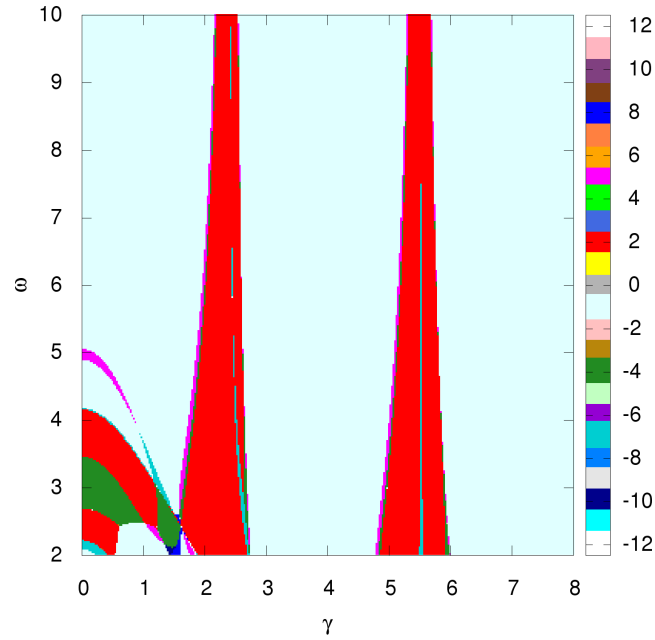

FIG. 13. The Chern number of the state with lowest energy of the central Floquet zone for a flux per unit cell of $p/q = 1/3$ and circularly polarized driving.

To assure the correctness of the topological invariant, we applied the algorithm proposed by Höckendorf *et al.* [42] to compute numerically the W_3 invariant for the Floquet-Hofstadter spectrum at $p/q = 1/3$. The result is plotted in Fig. 15. To have a comparison to the static topological invariants, we first compute the Chern number of the state with lowest energy of the central Floquet zone for a flux per unit cell of $p/q = 1/3$ and circularly polarized driving. The three-dimensional momentum-time BZ is discretized by $200 \times 200 \times 200$ points together with 30 Floquet replicas. The resulting Chern numbers are plotted in Fig. 13 for different amplitudes γ and frequencies ω of the driving field. In the left lower region of Fig. 13, inside the arc from $(\gamma, \omega) = (0.0\, eAa/\hbar, 5.1\, g/\hbar)$ to $(\gamma, \omega) = (1.9\, eAa/\hbar, 2.0\, g/\hbar)$, we cannot trust the numerical values. The reason can be understood by investigating the band

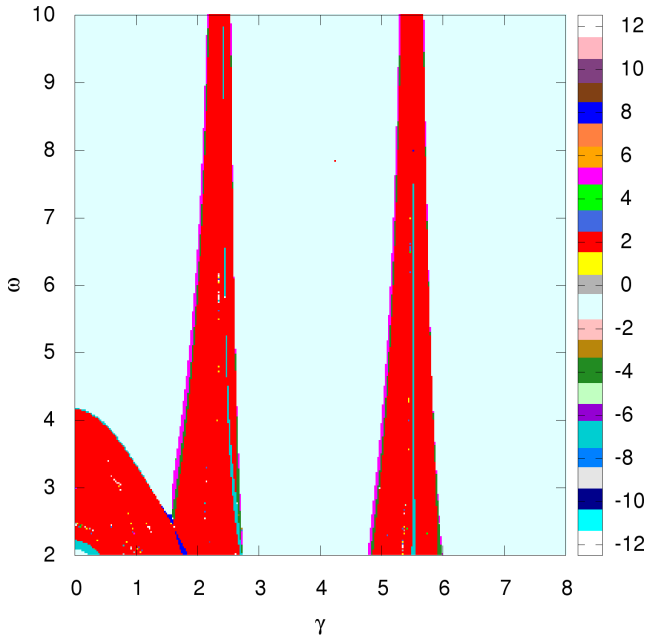

FIG. 14. The sum over all Chern numbers below $\varepsilon = 0$ computed from the truncated Floquet Hamiltonian with the same flux and polarization as in Figs. 13 and 15.

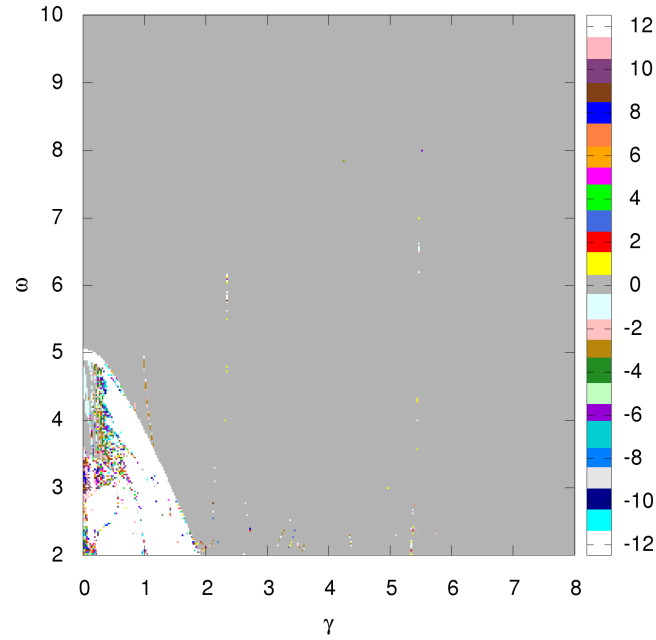

FIG. 16. The difference between the sum over Chern numbers and the W_3 invariant. Gray regions show parameter configurations (γ, ω) where the Chern number sum and the W_3 invariant coincide.

structure. In the parameter space where $\hbar\omega < 6.0\,g$, the bands of the Floquet-Hofstadter spectrum overlap and the Chern numbers are not well defined. With rising intensity, the degeneracies are lifted and anticrossings occur. Moreover, there are (γ, ω) regions where no gap between the lowest and the second lowest exists but the bands are nowhere degenerate, see Appendix A.

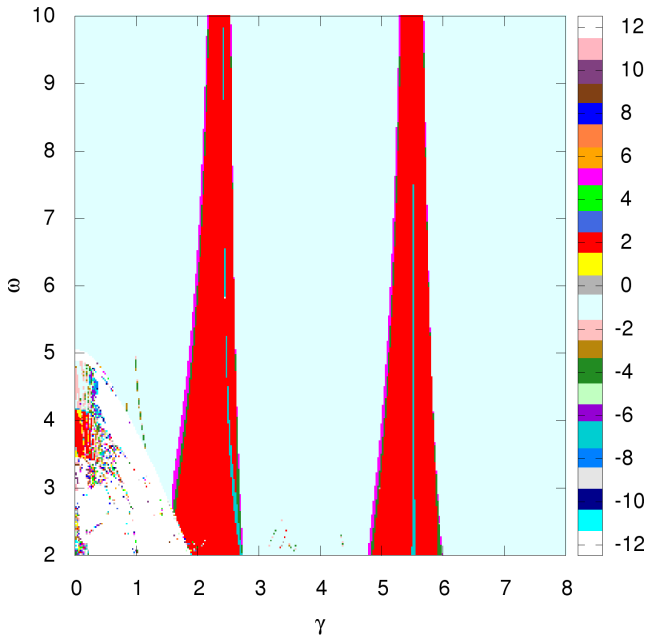

FIG. 15. The W_3 invariant computed with the algorithm by Höckendorf *et al.* [42] for the Floquet-Hofstadter spectrum at $p/q = 1/3$. The driving was circularly polarized.

In the last step, we apply the W_3 calculation scheme following Ref. [13], as mentioned before. The same flux and polarization is used as for Fig. 13. The result is plotted in Fig. 14. In the following, we compare the results of both W_3 calculations and contrast them against the corresponding Chern numbers.

The difference between both results for the W_3 invariant is depicted in Fig. 16. The comparison shows that apart from zones close to topological phase transitions, the results coincide. Interestingly, the Chern number itself also shows great agreement with both the sum over the Chern numbers and W_3. This justifies once more the topological characterization presented in Sec. IV A. Using the connection between edge modes and the W_3 invariant which has been proven in Ref. [13], this result allows for the prediction of the number of edge modes in this driven system.

Furthermore, we would like to stress that although the here-presented topological characterization is different from the one presented in Ref. [52] by Kooi *et al.*, the Chern numbers for a flux per unit cell of $p/q = 1/3$ agree with our results up to the sign of the W_3 invariants due to a different sign choice of the driving frequency.

V. SUMMARY

In this paper, we presented an explicit and rigorous treatment of the Hofstadter problem on the hexagonal lattice. One important result is the explicit proof of the periodicity of the Hofstadter butterfly: Depending on whether the numerator of the flux per unit cell is even or odd, the periodicity of the fractal spectrum is different. To understand how illumination of graphene with both circularly and linearly polarized light in the presence of a magnetic field will effect the fractal spectrum, we unified the Hofstadter butterfly with the Floquet

theory. These two polarization modes lead to clearly different scenarios. Circularly polarized light in combination with a magnetic field is able to lift the symmetry of the quasienergy spectrum around zero energy, whereas linearly polarized light is not, as shown by representative data. Furthermore, we investigated the gap size between different Floquet modes of the Floquet-Hofstadter spectrum.

To investigate the topological properties of this dynamical system, we studied the Chern number of the state with lowest quasienergy in the central Floquet mode for different flux values. Limiting the computations to the high-frequency regime, we were able to identify that the topological phase transitions induced by the external radiation field are only caused by gap closings and openings of butterfly bands and not by touching of different Floquet modes. For vanishing intensity the computed Chern numbers coincide with the ones of the undriven system. Furthermore, we found that the system undergoes several topological phase transitions when tuning the flux per unit cell or the intensity. Thereby, the distribution of the Chern numbers changes in the presence of an oscillating electric field for both linearly and circularly polarized light similarly. For moderate intensities, only a few Chern numbers are different from the Chern numbers of the static case whereas for higher intensities the distribution is substantially altered.

Yet the appropriate invariant to look at in case of a periodically driven system is the W_3 invariant. We computed this topological indicator for the Floquet-Hofstadter spectrum to give a comparison with the results on Chern numbers. In the high-frequency limit, both the Chern number and the W_3 invariant coincide, yielding the correct number of edge modes appearing in a system of finite size. The latter allows for experimental access. Finally, we were able to show agreement with other topology studies on the Floquet-Hofstadter spectrum in the off-resonant regime whereas our topology analysis of the system is valid in all driving regimes, resonant and off resonant.

Note added. Recently, other works on the same subject appeared, which stress the role of different regimes of the driving frequency. [52] and other lattice types [53].

ACKNOWLEDGMENTS

The authors thank V. Junk, P. Reck, K. Richter, B. Höckendorf, and A. Alvermann for various useful discussions. This work was supported by the Deutsche Forschungsgemeinschaft via GRK 1570 and Project No. 336985961.

APPENDIX A: GAPLESS NONDEGENERATE STATES

There is a global gap between two bands if the minimum of the upper band is always greater than the maximum of the lower band. Consider the case of two bands without a global energy gap. It does not imply that there is a degeneracy of the two bands. This scenario occurs for specific (γ, ω) configurations of the Floquet-Hofstadter spectrum between the lowest and second-lowest band marked as black stripes in Fig. 17. An exemplary quasienergy band structure is shown in Fig. 18. There is no gap between the lowest two nondegenerate bands.

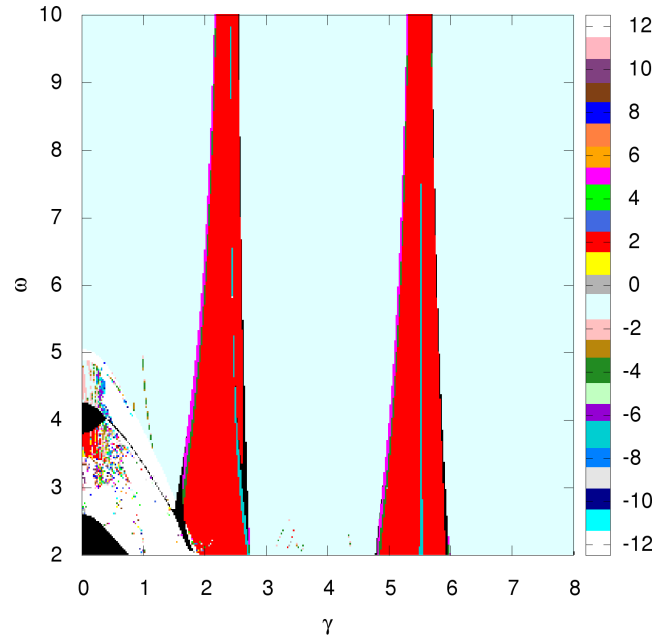

FIG. 17. The W_3 invariant computed with the algorithm of Höckendorf *et al.* [42] for the Floquet-Hofstadter spectrum at $p/q = 1/3$. The driving was circularly polarized. Parameter spaces (γ, ω) without a gap are marked black.

APPENDIX B: W_3-INVARIANT FOR GRAPHENE WITHOUT MAGNETIC FIELD

Although there are examples where the summation over the Chern numbers of the truncated Floquet Hamiltonian fails

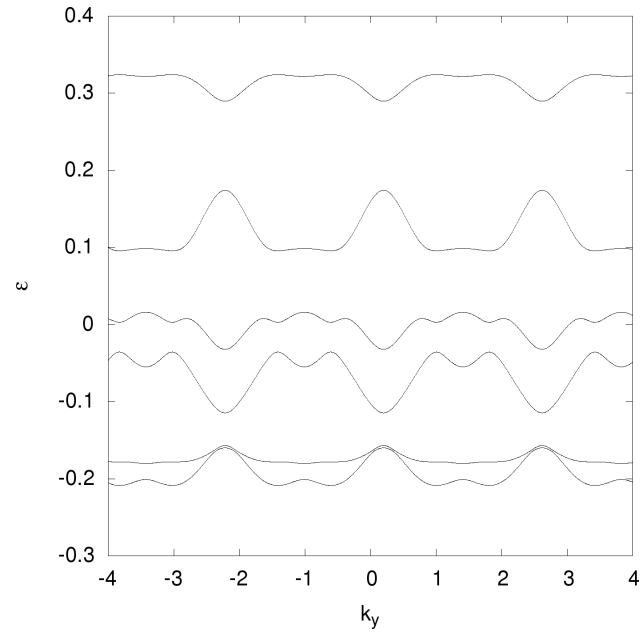

FIG. 18. The quasienergy band structure for $p/q = 1/3$, $(\gamma, \omega) = (2.65\, eAa/\hbar, 3.0\, g/\hbar)$ and $k_x = 0$. The lowest two bands are not degenerate but they do not have a gap in the sense that the minimum of the second lowest band is always greater than the maximum of the lowest band.

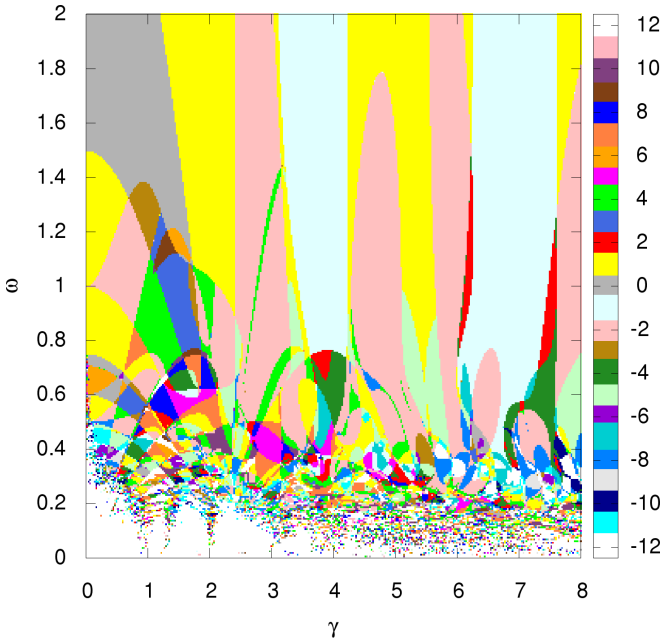

FIG. 19. The sum over all Chern numbers of the truncated Floquet Hamiltonian below $\varepsilon = 0$ for graphene with circularly polarized driving and without magnetic field. Our data almost perfectly reproduce the results from Ref. [14].

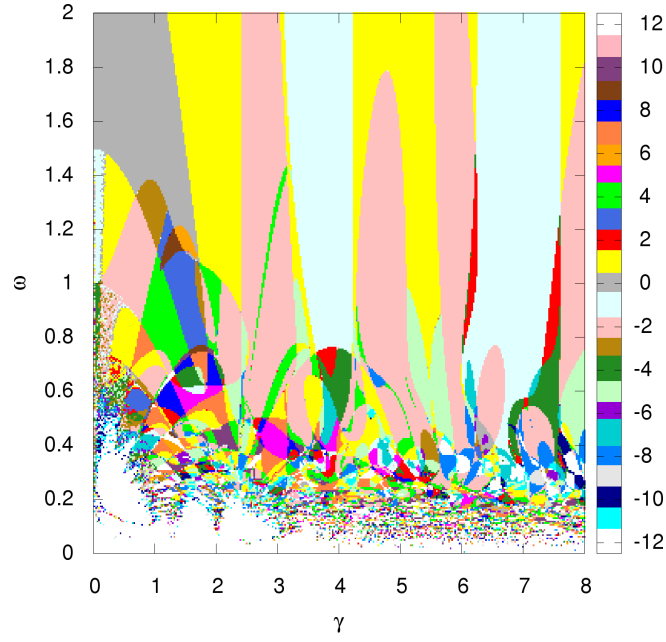

FIG. 20. The W_3 invariant coincides in reliable regions with the sum over Chern numbers. Except for numerical unstable regions, the Chern number sum and the W_3 invariant show a striking agreement.

to give the correct topological invariant, as shown, e.g., by two examples in Ref. [42], the procedure gives the correct results for several models including circularly polarized driven graphene. In the seminal work by Mikami *et al.* on Floquet topological insulators [14], the authors were able to relate topological phase transitions to effective hopping amplitudes. Moreover, the topological phase diagram of graphene with circularly polarized driving has been investigated. To make direct contact to the work by Mikami [14], we have set the discretization of the time-momentum BZ to $200 \times 200 \times 200$ and the number of Floquet replicas to 50. Although the lowest and topmost eigenvalues and eigenvectors of the truncated Floquet Hamiltonian are not converged, i.e., they are different from the index shifted eigenvectors with eigenvectors taken from the central Floquet zone [compare Eq. (45)], they remain relevant for the topological classification of driven graphene. In the converged Floquet zones, the sum over all bands has to be zero inside one specific Floquet zone [42]. For the lowest and highest Floquet zones, this is not necessarily the case. The deviation from the converged Chern numbers contains the information about the difference of Chern numbers and the W_3 invariants such that the summation indeed gives the correct topological invariant. This can be seen when comparing the sum over all Chern numbers of the truncated Floquet Hamiltonian Fig. 19 with the W_3 invariant Fig. 20. The difference between the two values is plotted in Fig. 25. In the region of small intensities γ and $\hbar\omega < 1.5\,g$, they do not agree. However, this is due to numerical instabilities of the algorithm for the W_3 invariant. To show that there is indeed no difference between the sum over Chern numbers and W_3, we analyzed the sizes of the gaps at zero quasienergy and $-\omega/2$. Figure 21 shows the difference between $-\omega/2$ and the minimum of the lower band of the central Floquet zone.

Comparing the regions where the $-\omega/2$-gap is closed with the corresponding regions where the Chern number changes, Fig. 26, one can see that the zeros of the $-\omega/2$-gap are responsible for a change of Chern numbers. Whereas, the arc in Fig. 22 starting from $(\gamma, \omega) = (0.5\,eAa/\hbar, 1.2\,g/\hbar)$ to $(\gamma, \omega) = (1.0\,eAa/\hbar, 1.36\,g/\hbar)$, where the zero gap is closed,

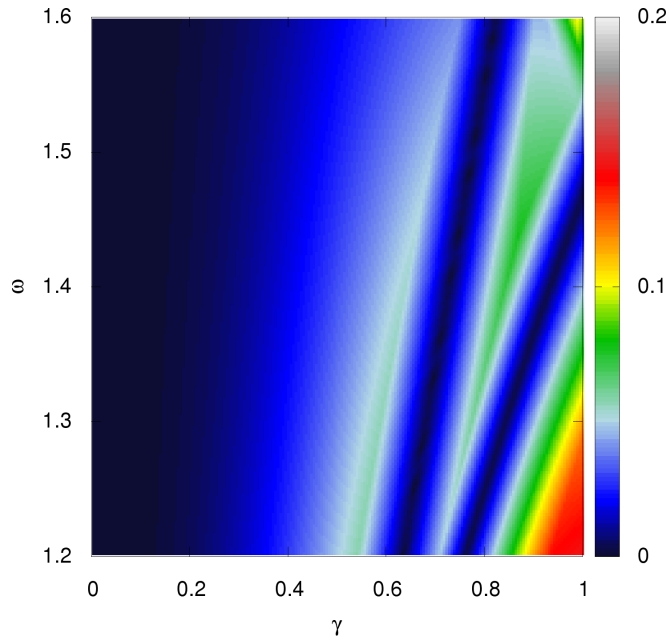

FIG. 21. The size of the zone edge gap in dependence of intensity γ and driving frequency ω. The data were calculated as distance between the minimum of the lower band of the central Floquet zone and $-\omega/2$. The zero lines at the right half of the plot are also visible as topological phase transition in Fig. 26.

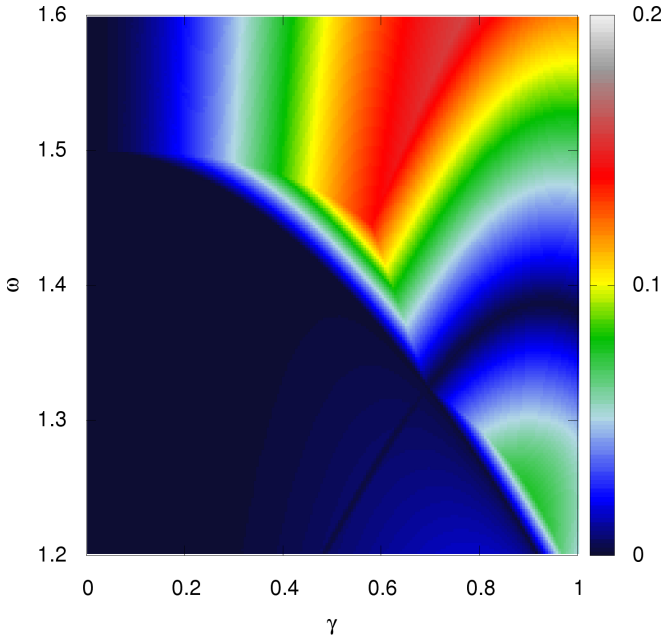

FIG. 22. The minimum of the upper band of the central Floquet zone in dependence of intensity γ and driving frequency ω is plotted. The zeros, and with the band touchings, can be directly mapped to a change of the sum over Chern numbers, compare Fig. 19.

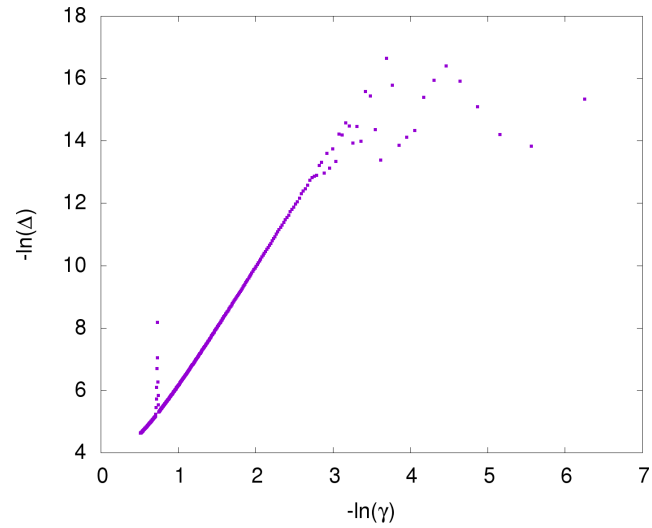

FIG. 23. Δ is the minimum of the upper band of the central Floquet zone and γ is here understood as dimensionless intensity $\gamma \to \gamma\,\hbar/eAa$. The plot shows the gap size, i.e., the difference between the minimum of the upper band and zero, for $\gamma = 1/520$ to $\gamma = 3/5$ at fixed $\omega = 1.2\,g/\hbar$. The peak at $-\ln(\gamma) \approx 0.7$ is an evidence for a gap closing at $\gamma = 0.5$. Whereas for $-\ln(0.2) \approx 1.6$, no peak is visible, giving a hint that there is no topological phase transition at $\gamma = 0.2$.

can be seen in Fig. 20 as well as in Fig. 26. In the following, we clarify if there is a difference between the sum over Chern number of the truncated Floquet Hamiltonian and the W_3 invariant. We calculated the gap sizes in the interval $\gamma \in [0.0, 0.6]\,eAa/\hbar$ for $\omega = 1.2\,g/\hbar$. The BZ is discretized by using 3500×3500 points. If there would be a gap closing, e.g., at $(\gamma, \omega) = (0.2\,eAa/\hbar, 1.2\,g/\hbar)$, in Fig. 20 we should see a signature of a gap closing either in Fig. 23 or in Fig. 24. The latter show the gap sizes in a double logarithmical plot for the zero and the $-\omega/2$ gap. If there would be a gap closing, there should be a signature at $-\ln(\gamma) \approx 1.6$ which is not the case. This shows that the deviations between Chern number summation and W_3 can be traced back to numerical instabilities. Indeed, we were able to achieve agreement between the results of the summation over Chern numbers and the W_3 invariant when increasing the discretization of the time-momentum BZ for some representative points. As an example, we investigated $(\gamma, \omega) = (0.1\,eAa/\hbar, 1.4\,g/\hbar)$: An increase of the number of discretization points to $800 \times 800 \times 800$ is necessary to achieve convergence of the W_3 algorithm and, with that agreement, with the summation over Chern numbers. Besides numerical demanding regions, both topological characterizations show a striking agreement, colored with gray in Fig. 25. To our knowledge, apart from the observation that the sum over the Chern numbers of the truncated Floquet Hamiltonian and the W_3 invariant seem to coincide for circularly driven graphene, a proof, so far, is missing. Remarkably, even in the cases where both the Chern number and the W_3 invariant coincide (e.g., compare $(\gamma, \omega) = (4.0\,eAa/\hbar, 2.0\,g/\hbar)$ Figs. 26 and 20), not all Floquet zones of the truncated Floquet Hamiltonian have the same Chern numbers as the central Floquet zone, as depicted in Fig. 27. This holds even for the off-resonant regime. Figure 28 extends Fig. 27 to higher driving frequencies. However, this feature survives for even higher driving frequencies $\omega \propto 10^6\,g/\hbar$. Again, this can be understood when having a closer look at the quasienergy band structure. In the far off-resonant regime, the gap between the two bands of graphene is very small. Hence, even when the Floquet zones are far away from each other, a small coupling is enough to close and reopen the small gap of some Floquet zones.

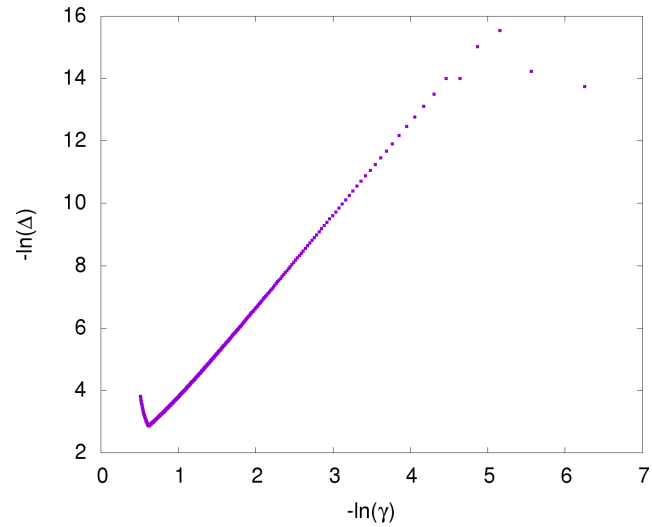

FIG. 24. Δ is the distance between the minimum of the lower band of the central Floquet zone and $-\omega/2$ and, as in Fig. 23, γ is again dimensionless. No peak is visible in this plot, where γ and ω are in the same parameter range as in Fig. 23.

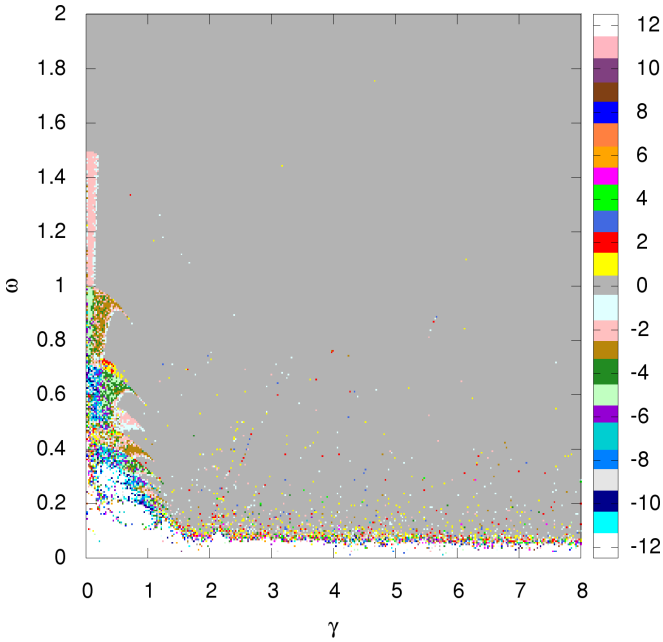

FIG. 25. Difference between the W_3 invariant and the sum over Chern numbers.

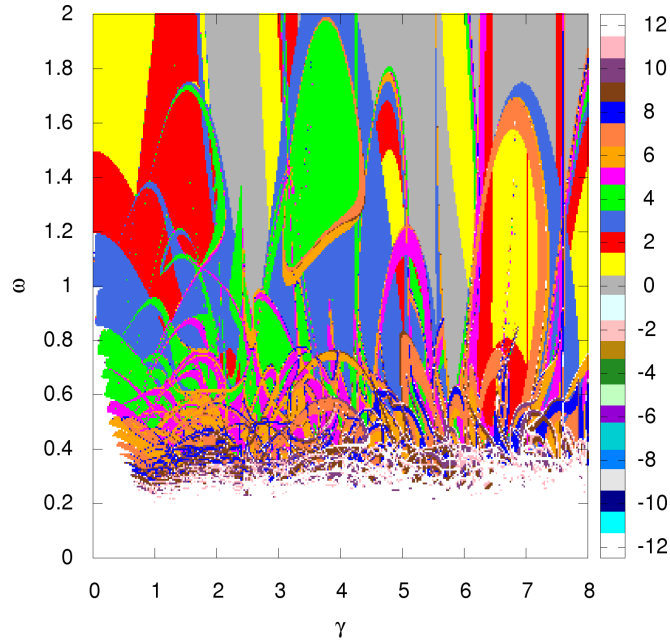

FIG. 27. The innermost Floquet zone having different Chern numbers from that of the central Floquet zone. The counting of the Floquet zones starts here with the lowest mode, e.g., for $(\gamma, \omega) = (4.0\, eAa/\hbar, 1.6\, g/\hbar)$ the $(-50{+}4)$th Floquet zone has different Chern numbers from the Chern numbers of the central Floquet zone.

APPENDIX C: W_3 INVARIANT FOR SPIN-1/2 ROTATIONS

Besides the example given in the main text, there is a second case given in Ref. [42], where the summation over the truncated Floquet Hamiltonian does not give the correct topological invariant in the driven case. In this case, the time-evolution operator reads

$$U(\vec{\mu}) = e^{-i2\pi w \vec{g}(\vec{\mu})\cdot\vec{\sigma}}, \tag{C1}$$

where $\vec{g}(\vec{\mu})$ is a bijective map from the cube $[0,1]^3$ to the unit ball $|\vec{\mu}| \leqslant 1$ that maps the surface (center) of the cube to the surface (center) of the unit ball [42]. Let us set $w = 1$ to calculate the W_3-invariant for one period. The mapping $\vec{g}(\vec{\mu})$

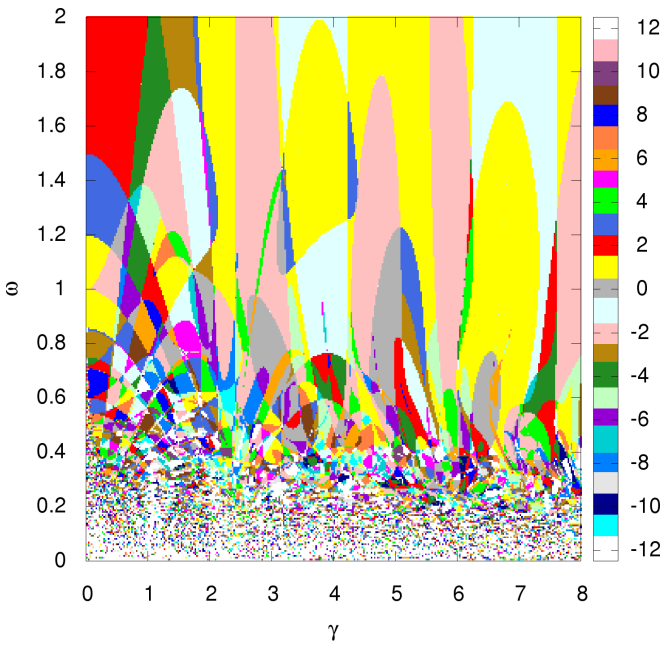

FIG. 26. The Chern number of the lower band of graphene of the central Floquet zone. The driving is again circularly polarized. One can see the difference to the W_3-invariant in Fig. 20.

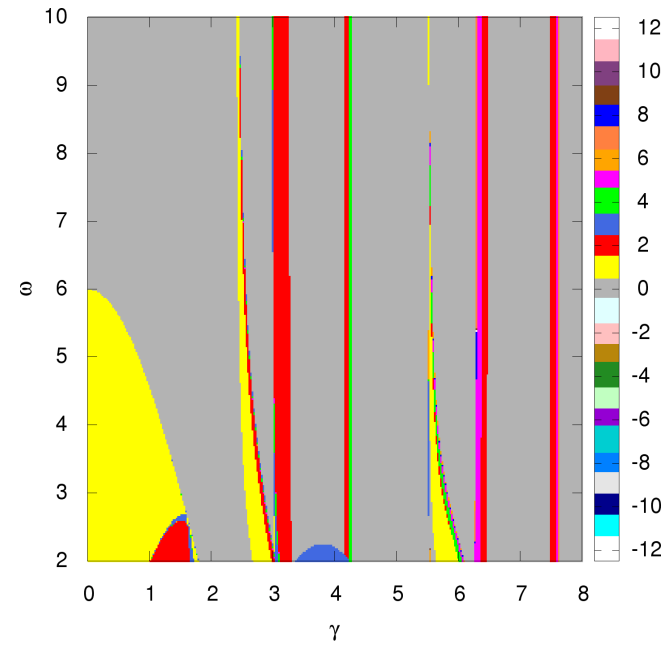

FIG. 28. Even in the far off-resonant regime, not all Chern numbers of the Floquet zones of the truncated Floquet Hamiltonian agree with the Chern numbers of the central Floquet zone.

can be constructed by applying two mappings. The first one is shifting the unit cube and stretching it,

$$\vec{s}(\vec{\mu}) : [0, 1]^3 \to [-1, 1]^3, \tag{C2}$$

$$\vec{s}(\vec{\mu}) : \begin{pmatrix} x \\ y \\ z \end{pmatrix} \mapsto \begin{pmatrix} 2x-1 \\ 2y-1 \\ 2z-1 \end{pmatrix}, \tag{C3}$$

and the second one is the mapping to the unit ball:

$$\vec{c}(\vec{\mu}) : [-1, 1]^3 \to \{|\vec{\mu}| \leqslant 1 : \vec{\mu} \in \mathbb{R}^3\}, \tag{C4}$$

$$\vec{c}(\vec{\mu}) : \begin{pmatrix} x \\ y \\ z \end{pmatrix} \mapsto \begin{pmatrix} x\sqrt{1 - \frac{y^2}{2} - z^2\left(\frac{1}{2} - \frac{y^2}{3}\right)} \\ y\sqrt{1 - \frac{z^2}{2} - x^2\left(\frac{1}{2} - \frac{z^2}{3}\right)} \\ z\sqrt{1 - \frac{x^2}{2} - y^2\left(\frac{1}{2} - \frac{x^2}{3}\right)} \end{pmatrix}. \tag{C5}$$

By concatenation, we yield

$$\vec{g}(\vec{\mu}) = \vec{c}\big(\vec{s}(\vec{\mu})\big). \tag{C6}$$

With the explicit form given for the mapping from the cube to the ball, we can calculate the eigenvalues of the operator $\vec{g}(\vec{\mu}) \cdot \vec{\sigma}$, which are

$$\lambda_\pm = \pm\sqrt{1 + 64xyz(x-1)(y-1)(z-1)}\,. \tag{C7}$$

By identifying $x \equiv k_x$, $y \equiv k_y$, and $z \equiv t/T$, the time-dependent Hamiltonian can be reconstructed with

$$H(t) = i\hbar\big(\partial_t U(t)\big)U^\dagger(t). \tag{C8}$$

Having $H(t)$, we can calculate the corresponding Floquet Hamiltonian which has a driving period of $\omega = 2\pi$ since we have chosen $w = 1$. But we know that the quasienergies $\varepsilon_\pm$ of the Floquet Hamiltonian are equal to the eigenvalues of $U(\vec{\mu})$ evaluated after one period, i.e.,

$$\varepsilon_\pm = i \ln e^{\pm i2\pi\lambda_\pm}|_{t/T=1}, \tag{C9}$$

$$= \pm 2\pi, \tag{C10}$$

and by shifting the quasienergies into the central Floquet zone we get two degenerate bands with zero quasienergy:

$$\varepsilon_\pm = 0. \tag{C11}$$

The Floquet spectrum is everywhere degenerate but the Chern numbers are well defined. However, the summation over Chern numbers of the truncated Floquet Hamiltonian doesn't give the correct topological invariant, which in this case is $W_3 = 2$.

[1] K. v. Klitzing, G. Dorda, and M. Pepper, Phys. Rev. Lett. **45**, 494 (1980).
[2] K. von Klitzing, Rev. Mod. Phys. **58**, 519 (1986).
[3] M. Z. Hasan and C. L. Kane, Rev. Mod. Phys. **82**, 3045 (2010).
[4] X.-L. Qi and S.-C. Zhang, Rev. Mod. Phys. **83**, 1057 (2011).
[5] D. R. Hofstadter, Phys. Rev. B **14**, 2239 (1976).
[6] D. J. Thouless, M. Kohmoto, M. P. Nightingale, and M. den Nijs, Phys. Rev. Lett. **49**, 405 (1982).
[7] T. Fukui, Y. Hatsugai, and H. Suzuki, J. Phys. Soc. Jpn. **74**, 1674 (2005).
[8] T. Oka and H. Aoki, Phys. Rev. B **79**, 081406(R) (2009).
[9] T. Kitagawa, E. Berg, M. Rudner, and E. Demler, Phys. Rev. B **82**, 235114 (2010).
[10] N. H. Lindner, G. Refael, and V. Galitski, Nat. Phys. **7**, 490 (2011).
[11] Z. Gu, H. A. Fertig, D. P. Arovas, and A. Auerbach, Phys. Rev. Lett. **107**, 216601 (2011).
[12] J. Cayssol, B. Dóra, F. Simon, and R. Moessner, Phys. Status Solidi (RRL) **7**, 101 (2013).
[13] M. S. Rudner, N. H. Lindner, E. Berg, and M. Levin, Phys. Rev. X **3**, 031005 (2013).
[14] T. Mikami, S. Kitamura, K. Yasuda, N. Tsuji, T. Oka, and H. Aoki, Phys. Rev. B **93**, 144307 (2016).
[15] M. Holthaus, J. Phys. B: Atm. Mol. Opt. **49**, 013001 (2016).
[16] J. Klinovaja, P. Stano, and D. Loss, Phys. Rev. Lett. **116**, 176401 (2016).
[17] J. Karch, P. Olbrich, M. Schmalzbauer, C. Zoth, C. Brinsteiner, M. Fehrenbacher, U. Wurstbauer, M. M. Glazov, S. A. Tarasenko, E. L. Ivchenko, D. Weiss, J. Eroms, R. Yakimova, S. Lara-Avila, S. Kubatkin, and S. D. Ganichev, Phys. Rev. Lett. **105**, 227402 (2010).
[18] H. L. Calvo, H. M. Pastawski, S. Roche, and L. E. F. F. Torres, Appl. Phys. Lett. **98**, 232103 (2011).
[19] Y. Zhou and M. W. Wu, Phys. Rev. B **83**, 245436 (2011).
[20] A. Scholz, A. López, and J. Schliemann, Phys. Rev. B **88**, 045118 (2013).
[21] G. Usaj, P. M. Perez-Piskunow, L. E. F. Foa Torres, and C. A. Balseiro, Phys. Rev. B **90**, 115423 (2014).
[22] M. A. Sentef, M. Claassen, A. F. Kemper, B. Moritz, T. Oka, J. K. Freericks, and T. P. Devereaux, Nat. Commun. **6**, 7047 (2015).
[23] A. López, A. Di Teodoro, J. Schliemann, B. Berche, and B. Santos, Phys. Rev. B **92**, 235411 (2015).
[24] Y.-X. Wang and F. Li, Physica B: Condensed Matter **492**, 1 (2016).
[25] A. López, A. Scholz, B. Santos, and J. Schliemann, Phys. Rev. B **91**, 125105 (2015).
[26] P. Mohan, R. Saxena, A. Kundu, and S. Rao, Phys. Rev. B **94**, 235419 (2016).
[27] M. Tahir, Q. Y. Zhang, and U. Schwingenschlögl, Sci. Rep. **6**, 31821 (2016).
[28] M. Claassen, C. Jia, B. Moritz, and T. P. Devereaux, Nat. Commun. **7**, 13074 (2016).
[29] A. López, Z. Z. Sun, and J. Schliemann, Phys. Rev. B **85**, 205428 (2012).
[30] A. López, A. Scholz, Z. Z. Sun, and J. Schliemann, Eur. Phys. J. B **86**, 366 (2013).
[31] R. Rammal, J. Phys. (France) **46**, 1345 (1985).
[32] Y. Hasegawa and M. Kohmoto, Phys. Rev. B **74**, 155415 (2006).
[33] J. Wang and J. Gong, Phys. Rev. Lett. **102**, 244102 (2009).
[34] J.-W. Rhim and K. Park, Phys. Rev. B **86**, 235411 (2012).

[35] F. Yilmaz, F. N. Ünal, and M. O. Oktel, Phys. Rev. A **91**, 063628 (2015).
[36] F. Yilmaz and M. O. Oktel, Phys. Rev. A **95**, 063628 (2017).
[37] J. K. Asbóth and A. Alberti, Phys. Rev. Lett. **118**, 216801 (2017).
[38] C. R. Dean, L. Wang, P. Maher, C. Forsythe, F. Ghahari, Y. Gao, J. Katoch, M. Ishigami, P. Moon, M. Koshino, T. Taniguchi, K. Watanabe, K. L. Shepard, J. Hone, and P. Kim, Nature **497**, 598 (2013).
[39] Y. H. Wang, H. Steinberg, P. Jarillo-Herrero, and N. Gedik, Science **342**, 453 (2013).
[40] S. Owerre, Ann. Phys. **399**, 93 (2018).
[41] B. Höckendorf, A. Alvermann, and H. Fehske, Phys. Rev. B **97**, 045140 (2018).
[42] B. Höckendorf, A. Alvermann, and H. Fehske, J. Phys. A: Math. Theor. **50**, 295301 (2017).
[43] F. Nathan and M. S. Rudner, New J. Phys. **17**, 125014 (2015).
[44] M. V. Berry, Proc. R. Soc. London A **392**, 45 (1984).
[45] B. Simon, Phys. Rev. Lett. **51**, 2167 (1983).
[46] N. Goldman, J. Phys. B: At., Mol. Opt. **42**, 055302 (2009).
[47] K. I. Seetharam, C.-E. Bardyn, N. H. Lindner, M. S. Rudner, and G. Refael, Phys. Rev. X **5**, 041050 (2015).
[48] R. Desbuquois, M. Messer, F. Görg, K. Sandholzer, G. Jotzu, and T. Esslinger, Phys. Rev. A **96**, 053602 (2017).
[49] More precisely, the following conditions have to be fulfilled [13]: 1) $\tilde{U}(\vec{k}, T) = \mathbb{I}$. 2) There should exist a one-parameter family of evolution operators $\{U_s : s \in [0, 1]\}$ which interpolates between U and $\tilde{U}$ as follows: $U_{s=0}(\vec{k}, t) = U(\vec{k}, t)$ and $U_{s=1}(\vec{k}, t) = \tilde{U}(\vec{k}, t)$. 3) $\tilde{U}(\vec{k}, T)$ has to maintain a gap around ε_s with $\varepsilon_{s=0} = \varepsilon$, $\varepsilon_{s=1} = \pi/T$ and a smooth interpolation from $s = 0$ to $s = 1$.
[50] J. H. Shirley, Interaction of a quantum system with a strong oscillating field, Ph.D. thesis, California Institute of Technology, 1963.
[51] J. H. Shirley, Phys. Rev. **138**, B979 (1965).
[52] S. H. Kooi, A. Quelle, W. Beugeling, and C. Morais Smith, Phys. Rev. B **98**, 115124 (2018).
[53] L. Du, Q. Chen, A. D. Barr, A. R. Barr, and G. A. Fiete, Phys. Rev. B **98**, 245145 (2018).